



Impedance spectroscopy study of Al/p-Cu₂ZnSnS₄ thin films Schottky diode grown by a two-stage method

Marwa Sebai¹ · Asma Hannachi¹ · Nicole Jaffrezic-Renault² · Mounir Kanzari^{1,3}

Received: 16 September 2023 / Accepted: 29 November 2023 / Published online: 24 December 2023
© The Author(s), under exclusive licence to Springer-Verlag GmbH, DE part of Springer Nature 2023

Abstract

In this paper, we report the electrical properties of Al/p-Cu₂ZnSnS₄ thin film Schottky diode fabricated by a two-step method. Cu₂ZnSnS₄ ingot was successfully grown by direct melting of the constituent elements, then (CZTS) thin film was grown using thermal evaporation method onto heated Mo substrate temperature at 100 °C. After that, the as-deposited CZTS sample were annealed in a sulfur atmosphere at 400 °C for 30 min. X-ray diffraction analysis reveals a polycrystalline CZTS preferentially oriented along a (112) plane in kesterite structure. For bulk material, the band gap energy is about 1.39 eV, the complex impedance plots display a semicircle with an equivalent circuit consisting of a parallel RC circuit connected to a series resistor. The CZTS thin film was investigated in the way of structural and electrical properties. Raman spectra ensured formation of kesterite CZTS phase. Dense and polycrystalline surface features were observed in SEM images of CZTS thin film. The I–V characteristics showed that a Schottky contact was obtained between Aluminum and p-Cu₂ZnSnS₄ absorber layer. Characteristic parameters such as saturation current, ideality factor and series resistance were calculated from the experimental I–V data. These parameters showed significant electrical properties such as low series resistance and an ideality factor between 1 and 2. Finally, the Arrhenius diagram provided a very low activation energy of about 2.03 meV.

Keywords Cu₂ZnSnS₄ · Impedance spectroscopy · Thin films · Schottky diode · I–V characteristics

1 Introduction

Over the past few years, Cu(In, Ga)(S, Se)₂ (CIGS) polycrystalline solar cells and CdTe solar cells have witnessed considerable progress to attain a rapid mass production [1–3].

The conversion efficiencies of the thin film solar cells such as chalcogenide-based CIGS-based have almost reached 23% [4]. Although both technologies present considerable progress technically, they are hampered by the toxicity of cadmium (Cd) and scarcity issues of tellurium (Te), indium (In) and gallium (Ga) [5–7].

To overcome this problem, CZTS-based thin films appear as a promising alternative to CIGS technology because of their abundant, no expensive and non-toxic composition for the environment [8–11]. Therefore, CZTS thin films have been extensively studied for many applications [12–16]. And, with p-type conductivity, an optimum bandgap ranging from 1.45 to 1.6 eV [17, 18] and a high absorption coefficient (10⁴ cm⁻¹), CZTS-based thin films can be used as an absorber layer in a solar cell [17, 18].

An extensive research program is also devoted to metal–semiconductor (MS) structures, because of their significant contribution to the design of efficient technological components [19–23]. Metal–semiconductor contacts are a key component of almost all semiconductor electronic [24–27] and optoelectronic devices. They are applied in integrated circuits, photovoltaic devices, light detectors [28], microwave diodes, field effect transistors (FETs) [29] and organic field effect transistors (OFETs) [30]. Among the most interesting properties of an MS interface is the height of the Schottky barrier (SBH). Electronic transport across the MS interface is controlled by the SBH, and is therefore of major importance for the proper operation of any

✉ Marwa Sebai
sebai.marwa11@gmail.com

¹ Laboratoire de Photovoltaïque et Matériaux
Semi-Conducteurs, Université de Tunis El Manar, École
Nationale d'Ingénieurs de Tunis, 1002 Tunis, Tunisie

² Institut des Sciences Analytiques (ISA), Université de Lyon,
UMR 5280, Villeurbanne, France

³ Laboratoire de Photovoltaïque et Matériaux
Semi-Conducteurs-ENIT, Université de Tunis, IPEITunis
Montfleury, Tunis, Tunisie

semiconductor device [31]. In particularly for thin film solar cells based CZTS absorber, Schottky diodes based on a Mo/CZTS/Al structure have proved to be a suitable candidate for determining the characteristics of the absorber layer [32, 33].

Although there are some of studies focused on Mo/p-CIGS/Al Schottky diode [34–36], there has been limited works on Mo/CZTS/Al Schottky diodes [37, 38]. Atasoy et al. [37] and Touati et al. [38] have recently fabricated Al/p-CZTS/Mo Schottky diodes and evaluated the performance of these diodes by I–V analysis measured at room temperature.

Table 1 provides a partial list of device properties estimated from the well-known Cheung function for several multi-component copper-based structured thin-film Schottky diodes. It can be noticed that the electrical properties of the diodes were significantly affected by the processing method, the intermediate layer at the metal–semiconductor junction, the total device resistance, the film quality, and the thermal processing parameters [39]. It has also been reported that increasing the deposition temperature can improve the physical properties of the deposited CZTS thin films [39].

The investigation of the I–V characteristics of CZTS Schottky diodes deposited at 100 °C can reveal interesting aspects about the current conduction or metal–semiconductor barrier formation mechanism. To our knowledge, it is the first study on the I–V properties of Mo/CZTS/Al Schottky diode processed at 100 °C.

Here, we describes the synthesis of CZTS powder by solid-state reaction. This process is simple to perform, the starting materials are often available at low cost and the reactions are “clean” [40–43]. This research aims to develop Al/p-CZTS/Mo Schottky junctions by **thermal vacuum evaporation (PVD)** technique at 100 °C. Structural properties were evaluated using X-ray diffraction and Raman spectroscopy, morphological properties were studied by scanning electron microscopy (SEM). The band gap energy value (E_g) was determined using a diffuse reflectance spectrum. The electrical properties of CZTS bulk materials were investigated for the first time using impedance spectroscopy measurements. Finally, in order to further establish the interfacial response and thermionic emission mechanisms in the Schottky junctions, current–voltage (I–V) characteristics and impedance spectroscopic measurements of Al/p-CZTS/Mo

Schottky diode were performed. This provides an understanding of the influence of substrate temperature on thin film characteristics.

2 Experimental details

2.1 Synthesis of CZTS powder

$\text{Cu}_2\text{ZnSnS}_4$ was obtained by reacting stoichiometric quantities of elements of 99.999% purity, namely copper (Cu), zinc (Zn), tin (Sn) and sulfur (S), using the direct fusion components. The ingot was grown in a quartz tube. The tube containing the pure elements was sealed under a 10^{-6} Torr vacuum, then placed in a programmable furnace (type Nabertherm-Germany).

By following an appropriate thermal profile, we obtained a gray $\text{Cu}_2\text{ZnSnS}_4$ ingot, Fig. 1a. It was then crushed into a fine powder [48]. The powder was then pressed to form a 1 cm diameter cylindrical pellet, which was then used for characterization. As described, this technique is useful, very simple and does not involve other chemical elements [40–43].

2.2 Schottky junction fabrication

The Molybdenum (Mo) back contact was obtained by DC magnetron sputtering. The p-CZTS thin films were deposited under vacuum at a pressure of 10^{-6} Torr by thermal evaporation on the Mo-coated glass substrates. In order to avoid ejection during evaporation, the material (0.15 g) was placed in a molybdenum crucible in boat form with uniform distribution. The substrates were placed at 15 cm above the source, so that their surfaces were perpendicular to the vapour flow, Fig. 1b. Typical as-deposited film thicknesses were in the 400 nm range. To improve film crystallinity, the p-CZTS/Mo thin films were then sulfurized under nitrogen flow at 400 °C for 30 min. The use of nitrogen allowed for minimal oxidation, while sulphur was used to avoid defects.

Once the CZTS/Mo films were formed, an aluminium Schottky contact was deposited on top of the CZTS sample by thermal evaporation in vacuum. Figure 1c describes the device thus formed (Al/p-CZTS/Mo).

Table 1 Summary of device parameters including series resistance, ideality factor and saturation current estimated from the Cheung function for Schottky diodes

| Device structure | Processing technique | R_s (Ω) | η | I_s (μA) | Ref |
|------------------|--|--------------------|--------|-------------------------|----------|
| ITO/p-CZTS/Ag | Direct-ink-coating techniques | 261 | 2.23 | 8.24 | [39] |
| Mo/p-CZTS/Al | Thermal evaporation method (PVD) | 21.61 | 1.46 | 0.829 | [38] |
| ZnS/p-CZTS/Al | Spray pyrolysis | 2100 | 11.4 | 30 | [44] |
| Mo/p-CZTS/Al | Sputter deposition | 2099 | 5.34 | 2.11 | [37, 45] |
| Al/p-CFTS/Mo | Thermal evaporation of CFTS | 22 | 1.48 | 0.489 | [46] |
| FTO/CIGS/Al | Close-spaced vapor transport technique | 93.7 | 3.47 | 190 | [47] |

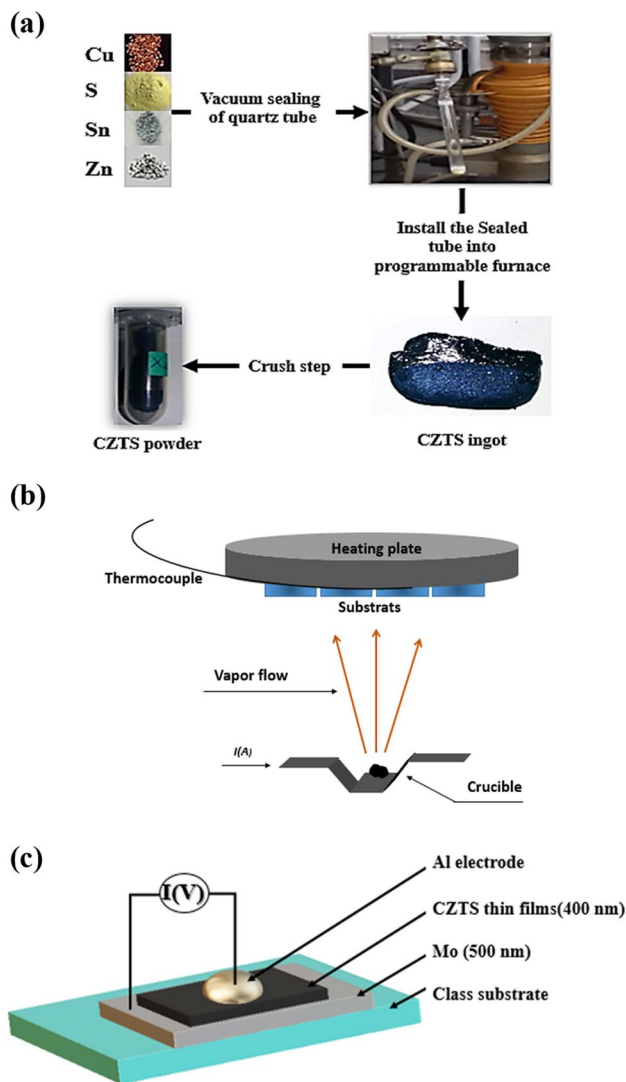


Fig. 1 **a** Schematics of the direct fusion method, **b** a schematic diagram of the PVD technique and, **c** schottky junction structure (Al/p-Cu₂ZnSnS₄/Mo)

2.3 Characterization

The X-ray diffraction analysis was carried out using Philips X'Pert X-ray diffractometer with monochromatic CuK α radiation ($\lambda = 1.5406 \text{ \AA}$). The band gap energy of the CZTS powder was obtained from diffuse reflectance spectroscopy (DRS) analysis over the wavelength range of 300–1800 nm at room temperature. Film thickness was determined by the interference fringe method [49]. Impedance measurements were carried out over a wide range of temperatures (573–653 K) and frequencies (5 Hz–13 MHz) using a Hewlett-Packard HP 4192 impedance analyzer. The measurements were carried out using two electrodes painted on both ends of the CZTS pellet with silver paste.

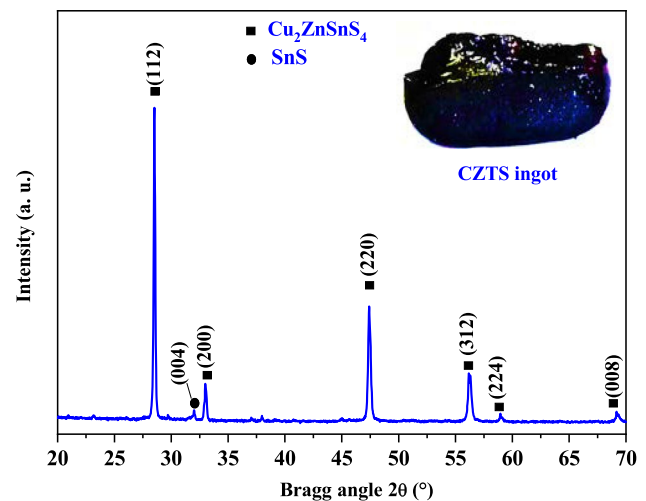


Fig. 2 X-ray diffraction pattern of CZTS powder

CZTS thin film was examined by X-ray diffraction (XRD) and Raman spectroscopy. The conductivity type was established by the hot probe method [49]. I–V characteristics of the Al/p-CZTS/Mo Schottky junction were recorded using an Agilent N6762A, and C–V measurements were made at room temperature using a low-frequency impedance analyzer (HP 4192A). The Schottky junction capacitance was also studied using a low-frequency impedance analyzer (HP 4192A).

3 Results and discussion

3.1 Structural properties of powder/X-ray diffraction

The XRD pattern of the synthesized Cu₂ZnSnS₄ is shown in Fig. 2, with clear diffraction peaks indicating that CZTS powder is polycrystalline. The main peaks are located at 28.58° , 33.01° , 47.41° , 56.11° , 58.94° and 69.18° , related to the (112), (200), (220), (312), (224) and (008) planes, corresponding to the kesterite structure according to JCPDS sheet No.: 00-026-0575. In addition, a peak located at $2\theta = 31.95^\circ$ derived from the (004) plane is observed, which could be attributed to the secondary SnS phase (JCPDS sheet N°: 00-053-0526). The average grain size (D) is determined using the Debye–Scherrer formula from the total width at half-maximum (FWHM) corresponding to the lattice planes of preferred orientation (112) and (220) [38].

$$D = \frac{0.9\lambda}{\beta \cos \theta}, \quad (1)$$

Table 2 The position of (112) and (220) peak, FWHM and the average crystallite size of CZTS powder and Schottky diode

| | 112 peak position | | | 220 peak position | | |
|----------------|---------------------|---------------------|--------|---------------------|---------------------|--------|
| | $2\theta(^{\circ})$ | FWHM ($^{\circ}$) | D (nm) | $2\theta(^{\circ})$ | FWHM ($^{\circ}$) | D (nm) |
| Powder | 28.51 | 0.15 | 51.2 | 47.41 | 0.23 | 37.84 |
| Schottky diode | 28.39 | 0.70 | 11.72 | 46.99 | 0.77 | 11.27 |

Table 3 Estimated values of dislocation density (δ_{dis}) and the strain (ϵ) of CZTS powder and thin film

| CZTS | $2\theta_{(112)}(^{\circ})$ | $\delta_{\text{dis}} (10^{-3} \text{ nm}^{-2})$ | $\epsilon (10^{-2})$ |
|----------------|-----------------------------|---|----------------------|
| Powder | 28.51 | 1.230 | 3.63 |
| Schottky diode | 28.39 | 2.956 | 0.295 |

where D is the average crystallite size and λ is the wavelength of X-ray employed. The parameters β and θ are the full-width at half maximum (FWHM) and the Bragg angle of (112) and (220) peaks of the CZTS compounds. Table 2 gives the calculated values of (D) and (FWHM) for the (112) and (220) peaks respectively. Crystal size values reported for the (112) plane are very close to those observed in the used standard cards and in the previous works [50–53], with a small variation explained by the different elaboration methods. Moreover, the decrease in crystal size between the (112) and (220) planes can be explained by the decrease in peak intensity.

Lattice deformation (ϵ) and dislocation density (δ_{dis}) are defined respectively as the lattice disarrangement created during the deposition process and the length of dislocation line per unit crystal volume, and were determined using the relation of Scherrer [53].

$$\epsilon = \frac{\beta \cos \theta}{4}, \quad (2)$$

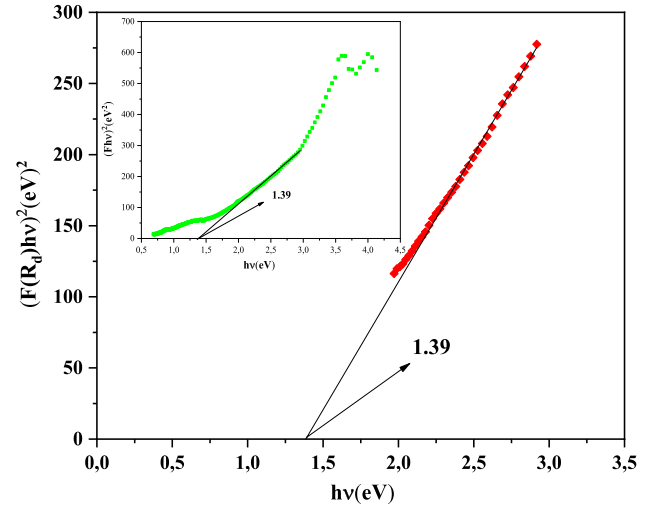
$$\delta_{\text{dis}} = \frac{1}{D^2}. \quad (3)$$

Strain and dislocation density were found to be $3.63 \cdot 10^{-2}$ and $1.23 \cdot 10^{-3} \text{ nm}^{-2}$ respectively (see Table 3).

3.2 Determination of band gaps of CZTS powder by Kubelka–Munk model:

The band gap energy value (E_g) of the CZTS bulk material was determined by exploiting the diffuse reflectance spectrum according to the Kubelka–Munk function [54, 55]:

$$F(R_d) = \frac{(1 - R_d)^2}{2R_d}. \quad (4)$$

**Fig. 3** Direct band gap of CZTS powder

The optical gap value E_g can be approximated based on the Kubelka–Munk model associated with the Tauc relation [56]:

$$((F(R_d)hv)^2 = A(hv - E_g), \quad (5)$$

$h\nu$ represents the energy of the incident photon and A is a constant. The direct determination of the bandgap energy is described elsewhere [57]. The resulting E_g value is 1.39 eV for CZTS compounds, Fig. 3. This value is in good agreement with the literature [58].

3.3 Electrical properties of CZTS powder

Impedance spectroscopy offers interesting information to understand the different relaxation phenomena and to correlate the electrical properties with the material structure [59].

The prepared pellet was then subjected to a series of complex impedance studies over a wide range of frequencies and temperatures to determine its relative electrical conductivity. To provide a more detailed illustration of the electrical conduction and transport mechanism, Nyquist diagrams are shown in Fig. 4a as a function of temperature, by plotting the complex impedance Z'' versus Z' . The observed diagrams reveal two distinct phases: a high-frequency phase due to the contribution of grain boundaries, and a low-frequency

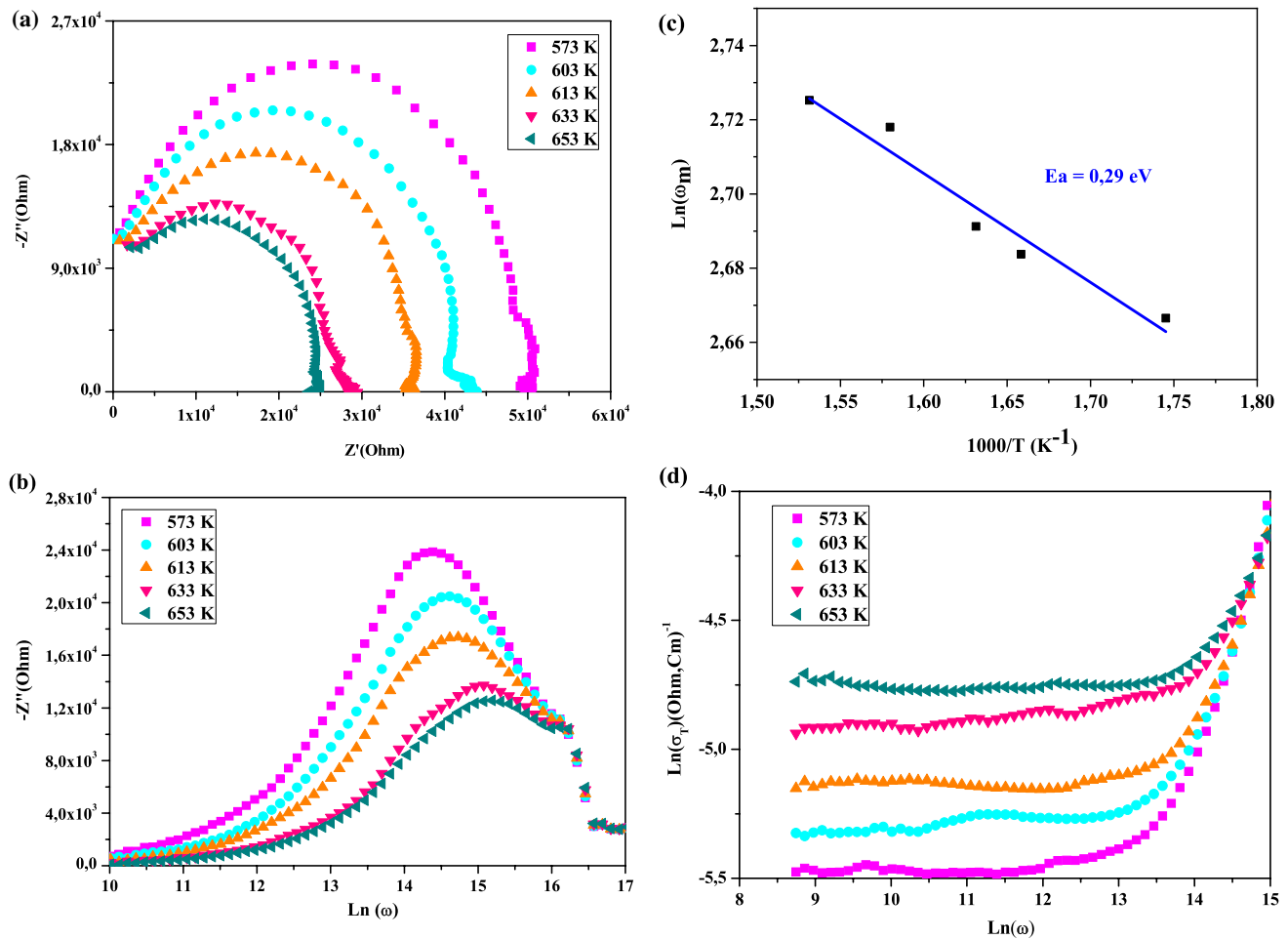


Fig. 4 Electrical properties of CZTS powder, **a** Nyquist diagram at different temperatures, **b** angular frequency dependence, **c** variation of $\ln(\omega_m)$ versus $(1000/T)$ and **d** frequency dependence of the total conductivity of the CZTS material

phase due to the contribution of grains in the conductivity mechanism [60–62].

The evolution of the imaginary part Z'' shown in Fig. 4b involves the appearance of one peak at each temperature with a particular frequency f_{\max} , which can be considered as the relaxation (resonance) frequency [58]. For low temperature values, the relaxation is predominant. A shift of the maximum peak Z'' to a higher frequency is also observed with increasing temperature. The maximum of the angular frequency is directly correlated to the relaxation time τ according to the formula $\pi f_{\max} \tau = 1$.

Such results represent additional proof of the semiconducting nature of the CZTS material and the contribution of carriers to the relaxation process [63]. The electrical conductivity and the relaxation time of CZTS compounds are thermally activated and appear to follow Arrhenius' law, as shown in Fig. 4b. The variation of the maximum peaks of the relaxation angular frequency $\omega_m = 2\pi f_{\max}$ with temperature complies with the Arrhenius law according to the following formula [64]:

$$\omega_m = \omega_0 e^{\frac{-E_a}{TK_b}}, \quad (6)$$

where ω_0 is a constant, E_a is the activation energy, T is the temperature and K_b is the Boltzmann constant. Figure 4c illustrates the variation of $\ln(\omega_m)$ as a function of $1000/T$. As indicated, the spectra of $\ln(\omega_m) = f(1000/T)$ show a linear characteristic. Using the same Eq. (6), the activation energy was found to be around 0.29 eV.

The measurement of AC conductivity was widely exploited to study the nature of defect centers in disordered systems, since they are assumed to be the origin of this conduction. The total conductivity (σ_T) as a function of the applied frequency is shown in Fig. 4d and can be written as follows [65, 66].

$$\sigma_T(\omega) = \sigma_{DC} + \sigma_{AC}, \quad (7)$$

where σ_{AC} and σ_{DC} are respectively the AC and DC conductivities.

At low angular frequency, σ_T shows a low frequency dependence and then it increases with increasing frequency, suggesting a DC contribution. The typical plot of $\ln(\sigma_T)$ versus $\ln(\omega)$ at different temperatures is shown in Fig. 4d. It can be seen that the AC conductivity shifts to a higher frequency with temperature, which is consistent with the observed change in relaxation frequency. This suggests that the conductivity is thermally activated. It is also an indication of high frequency hopping conduction between localized states [67].

3.4 Structural and morphological properties of Al/p-CZTS/Mo Schottky diode

The X-ray diffraction pattern of CZTS thin film is presented in Fig. 5a. It can be recognized that the diffraction pattern of the film is highly predominated by the (112) ($2\theta = 28.39^\circ$) and (220) ($2\theta = 47.07^\circ$) peaks at the expected locations of the CZTS kesterite phase planes (JCPDS 26-0575) [68]. Two diffraction peaks were found at $2\theta = 13.97^\circ$ and $2\theta = 40.64^\circ$ associated with the MoS_2 phase (JCPDS 98-004-3560) [69] and (Mo) (JCPDS card no. 42-1120), respectively. Actually, Mo has mainly served as a back contact for Cu-based chalcogenides (Table 1). However, the main problem associated with Mo is the formation of MoS_2 at the interface [70, 71]. During the sulfurization process by high-temperature annealing [72–74], an interface layer of MoS_2 is formed between the CZTS absorber and the Mo electrode [75]. The presence of MoS_2 peaks shows that sulfur has been deeply incorporated into the precursor film, suggesting significant sulfurization [37].

Table 2 shows an increase in FWHM and a decrease in crystallite size between the (112) and (220) planes for CZTS thin film. This decrease in crystallite size can be explained by the decrease in peak intensity and the widening of the (220) peak.

In the other hand, we report a decrease in crystallite size between CZTS bulk materials and CZTS thin films (Table 2). Actually, several basic factors explain the main differences between films and bulk materials, such as the variation in microstructures produced by deposition, nucleation and growth processes, the effect of interfaces on the film surface, and in particular, the nature of the substrate. Milton Ohring reported that the very high nucleation rate of grains that develop from condensed vapour at low temperatures leads to thin film grain sizes hundreds to thousands of times smaller than those that form in typical bulk materials [76]. Also, the powder diffractogram of a polycrystalline material does not show lattice stress and the peaks are very fine. In the case of CZTS thin-film materials, lattice variations caused by stress and structural defects due to the appearance of secondary Mo and MoS_2 phases result in a larger diffraction profile and degraded crystallinity.

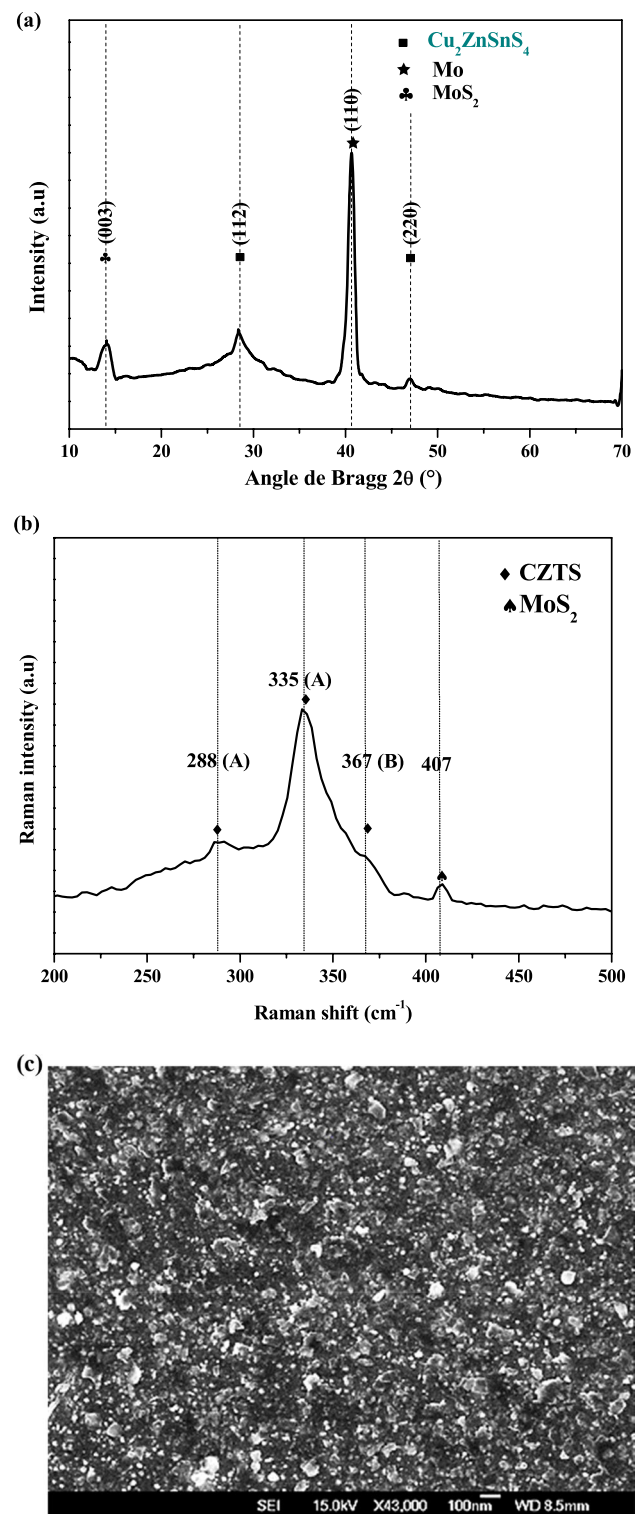


Fig. 5 Structural and morphological properties of CZTS thin films, **a** XRD pattern, **b** Raman spectra and **d** SEM top view of CZTS sample

As shown in Table 3, the dislocation density (δ_{dis}) and strain (ϵ) depend inversely on crystallite size. Decreasing crystallinity reduces the diffusion length of majority carriers and

increases carrier recombination in grain boundaries, resulting in lower conductivity.

We must note that these XRD peaks overlap with those of Cu₂SnS₃ and ZnS, so CZTS crystallization may not be confirmed by XRD analysis alone. Thus, Raman spectroscopy was carried out to gain a better understanding of phase identification. Raman spectroscopy is also being used to assess crystal quality and identify secondary phases in CZTS thin films [77, 78].

As shown in Fig. 5b, the Raman spectrum of Cu₂ZnSnS₄ indicated that the main Raman peak is located at 335 cm⁻¹ which may be the result of S atoms vibrations associated to the A1 symmetry planes [79]. The other peaks of the CZTS phase were signed in the figure. The spectrum also shows a smaller peak at 407 cm⁻¹ associated with the MoS₂ phase. Compared to previous results, the obtained structure seems to be more homogeneous and contains fewer secondary phases according to our Raman results [65].

The surface SEM micrograph is illustrated in Fig. 5c. The microstructure of the film surface is clearly dense, rough and polycrystalline.

3.5 Electrical property of Al/p-CZTS/Mo Schottky diode

3.5.1 Current–voltage (I–V) characteristics

Current–voltage (I–V) analysis as a function of temperature is one of the most commonly used methods for determining current conduction mechanisms through Schottky barrier diodes. This approach provides direct information on the type of barrier formed at the interface surface. The I–V performance of Al/p-CZTS/Mo Schottky junctions was evaluated using forward and reverse bias voltage at room temperature (~300 K). As highlighted in Fig. 6, the I–V curve of the junction shows rectifying behaviour which acts as a Schottky diode. In addition, the current varies exponentially at low voltage, implying thermionic emission conduction [38, 46]. According to this theory, the current in such a device can be expressed as [80]:

$$I = I_0 \left[\exp \left(\frac{q}{\eta K_B T} (V - R_s I) \right) - 1 \right], \quad (8)$$

where q is the carrier unit charge, η is the diode ideality factor, K_B is the Boltzmann constant, T is the absolute temperature, V is the applied voltage, R_s is the series resistance, and I_0 is the saturation current given by [38]:

$$I_0 = AA^* T^2 \exp \left(-\frac{q\phi_{B0}}{KT} \right). \quad (9)$$

A represent the diode contact area, A^* is the Richardson constant ($A^* = 63.6 \text{ A/cm}^2 \text{ K}^2$ for CZTS [38]) and ϕ_{B0} is the zero-bias barrier height.

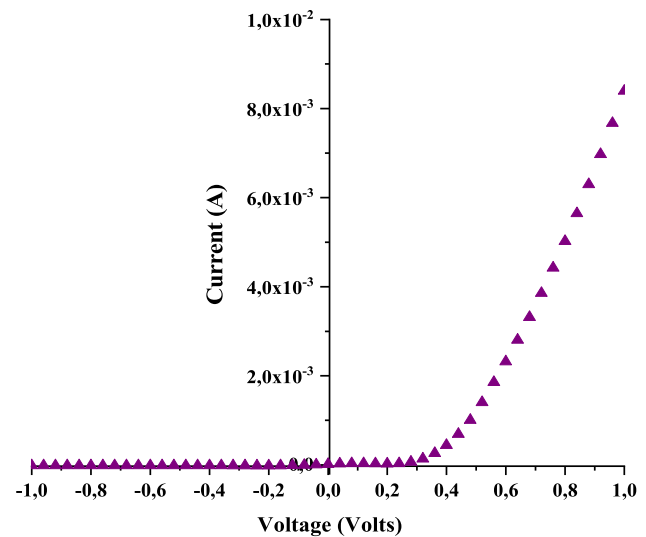


Fig. 6 Experimental forward and reverse bias current–voltage characteristics of the Al/p-CZTS/Mo Schottky junction

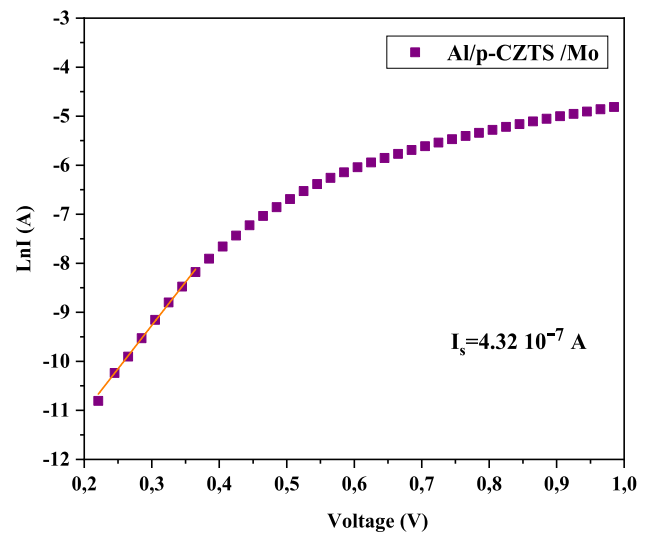


Fig. 7 Logarithm of the current density $\text{Ln}(I)$ versus the forward bias voltage (V) of Al/p-CZTS/Mo Schottky junction at room temperature

Up to the threshold potential, Eq. (8) can be written in logarithmic form as [80]:

$$\text{Ln}(I) = \text{Ln}(I_0) + \frac{q}{\eta K_B T} (V - R_s I). \quad (10)$$

As indicated in Fig. 7 and following the logarithmic form of Eqs. (8) and (10), the saturation current is calculated from the extrapolation of the linear region of the semi-logarithmic forward bias I–V curves at zero applied voltage (straight line derivative of the plot $\text{Ln} = f(V)$ at

$V = 0$). The calculated value of I_0 from the intercept of $\ln I = f(V)$ at $V = 0$ is found to be about $4.32 \cdot 10^{-7}$ A.

The ideality factor was introduced to explain the divergence between experimental I–V data and the predictions of ideal thermionic emission (TE) theory. When η is equal to one, pure thermionic emission occurs. However, η has usually a value greater than unit. The high values of η are derived from several effects, specifically film thickness inhomogeneity's, interface states, series resistance, defect states in the semiconductor bandgap [81, 82], and the non-uniformity in the interfacial charge distribution. The high ideality factor is usually associated with defective states in the semiconductor bandgap [38]. The values of η are estimated from the slope of the linear region of the forward bias I–V characteristics using the following relation:

$$\eta = \frac{q}{KT} \frac{dV}{d(\ln(I))}. \quad (11)$$

Figure 8 shows (a) $dV/d\ln(I)$ and (b) $H(I)$ versus current, respectively for the Al/p-CZTS/Mo Schottky structure. A linear behavior is thus obtained (Fig. 8a), and η is extracted accordingly. In the present study, η was found to be about 1.53.

Some research groups have studied the parameters of Mo/CZTS/Al diodes at room temperature. Rakhshani and Thomas [83] found $\eta = 4.5$, Touati et al. [38] found $\eta = 1.56$ and Atasoy et al. [37] found $\eta = 5.34$. Those values are higher than those obtained in this work ($\eta = 1.53$), which shows an improvement in the performance of this diode.

The Schottky barrier height (SBH) ϕ_{B0} can be evaluated using the following expression:

$$\phi_{B0} = \frac{KT}{q} \ln \left(\frac{A^* AT^2}{I_0} \right). \quad (12)$$

The barrier height ϕ_{B0} was found to be 0.689 eV. Some research groups have evaluated the parameters of Schottky Mo/CZTS/Al diodes at room temperature and reported that ϕ_{B0} were 0.71 eV according to Rakhshani and Thomas [83] while Rim et al found that $\phi_{B0} = 0.807$ eV [38], which is slightly higher than our values.

As well, making electrical contacts on the semiconductor generally involves the presence of a resistance called the contact resistance, depending on the nature of the contact, the type of metal and its design. This electrical resistance is coupled to the resistance of the semiconductor. The diode's series resistance " R_s " is therefore the combined result of all these resistances; it is connected in series with the ideal diode in the electrical circuit. The existence of a series resistor (R_s) severely degrades the device's performance and leads to a deterioration in electrical performance [39]. Cheung and Cheung [84, 85] assessed the series resistance

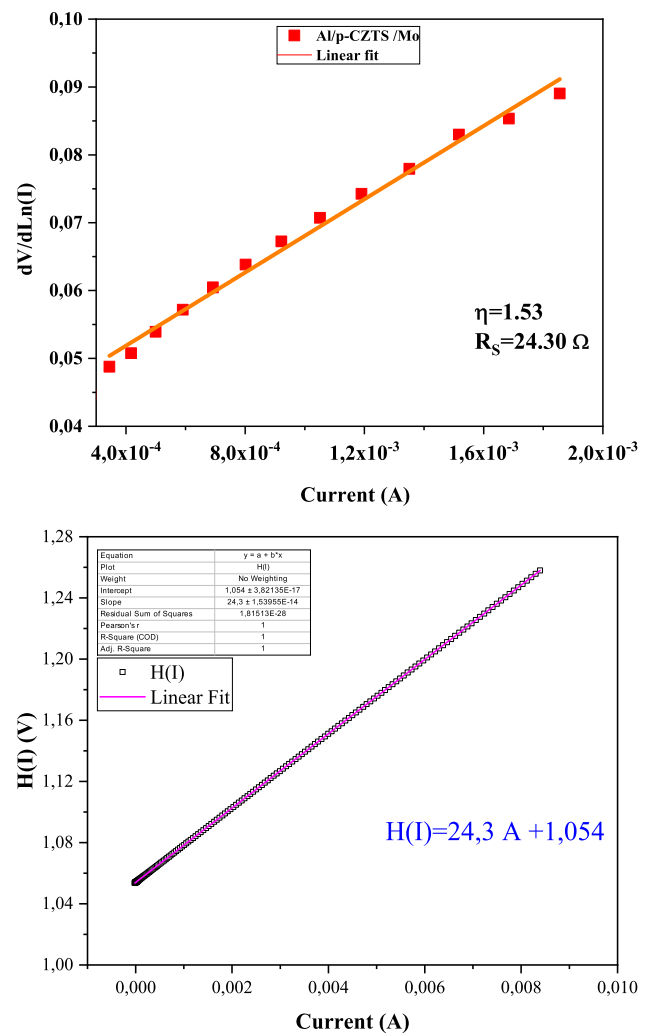


Fig. 8 a Experimental plot of $dV/d\ln(I)$ versus I and, b The experimental plot of $H(I)$ vs I , obtained from forward and reverse bias current–voltage characteristics of the Schottky structure (Al/CZTS p-type/Mo)

R_s using the developed model. Cheung's functions can be written as follows:

$$\frac{dV}{d(\ln I)} = R_s I + \frac{\eta KT}{q}, \quad (13)$$

$$H(I) = V - n \left(\frac{KT}{q} \right) \ln \left(\frac{I}{AA^* T^2} \right), \quad (14)$$

and

$$H(I) = IR_s + n\phi_b. \quad (15)$$

The barrier height and series resistance values found from Eq. 13 were respectively 0.71 eV and $24.30 \, \Omega$. Similarly, the values of the ideality factor and series resistance from Eq. 15 are 1.48 and $24.3 \, \Omega$, respectively. Thus, it can clearly

be seen that there is no significant difference between the values of n obtained from the downward curvature regions of forward bias I–V plots and from the linear regions of the same characteristics [85]. This agreement can be explained by the absence of series resistance effects and by the lack of polarization dependence of the Schottky contact on the voltage drop in the interfacial layer. Furthermore, the R_s values obtained from Eqs. 13 and 15 are the same, due to the consistency of the Cheung functions.

The resulting value of R_s is significantly lower than those found by Ghediya et al. ($R_s = 261 \Omega$) [39], Boutebakha et al. ($R_s = 2100 \Omega$) [44], Atasoy et al. ($R_s = 2099 \Omega$) [37] and significantly similar to that found by Touati et al. ($R_s = 21.61 \Omega$) [38]. This means that there is a clear improvement in the performance of the produced diode as compared to those produced previously using the same type of semiconductor.

3.5.2 Impedance spectroscopy

The complex impedance of (Al/p-CZTS/Mo) heterostructure was measured over a wide range of frequencies and temperatures. Figure 9a depicts the complex impedance of the imaginary part ($-Z''$) versus the real part (Z') of the deposited Al/p-CZTS/Mo, called the Nyquist plot.

The spectra present one semi-circular arc from which we can retrieve all characteristics namely relaxation time, resistance and capacitance. These observations present the response to excitatory electric fields applied to the sample and correspond to intergranular polarization phenomenon occurring at higher frequencies.

The analysis of experimental data (Fig. 9a) show one semi-circular arc from for each temperature, the semi-circles are slightly depressed and their maximum shift to higher frequencies as the temperature increases. The diameter and the maximum of the semicircles decrease with increasing temperature. This observation leads to the conclusion that the electrical conductivity is thermally activated as well as the relaxation times distribution [86, 87].

In the other hand, each semicircle can be fitted as an equivalent circuit consisting of a single parallel network of resistor R_p and capacitor C_p connected to a series resistor R_s . The equivalent circuit was established using EC-Lab software. The modelled equivalent circuit of this diode is shown in Fig. 9b. Where $Z(f)$ follows the following formula.

$$Z(f) = \frac{R_p}{1 + j2\pi f R_p C_p}. \quad (16)$$

In order to explore the relaxation time as a function of temperature, we plot Z'' versus frequency at various temperatures as shown in Fig. 9c. The graph are highlighted by the occurrence of a particular peak at f_{\max} for each temperature, which could be described as the relaxation frequency

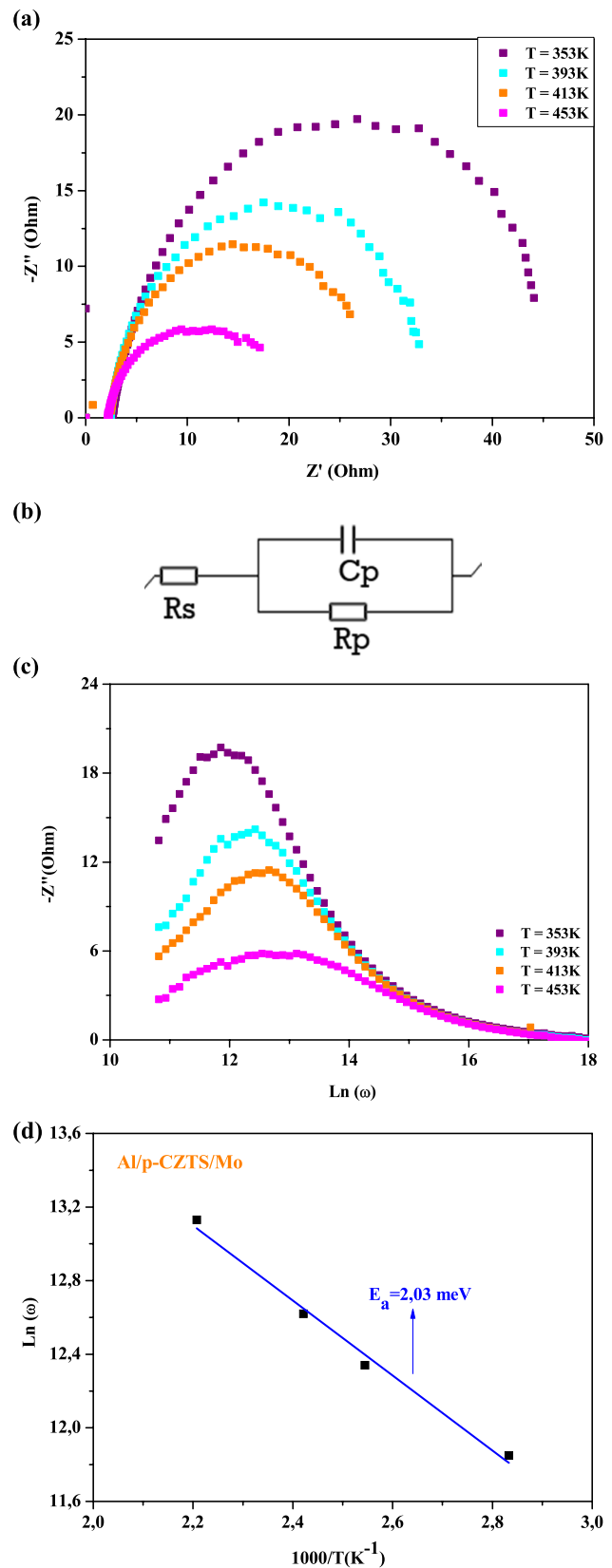


Fig. 9 Electrical properties of Al/p-CZTS/Mo Schottky diode, **a** Nyquist plots, **b** equivalent circuit, **c** angular frequency dependence and **d** Arrhenius diagram of the cut-off frequency for Al/p-CZTS/Mo Schottky diode

(resonance). Relaxation is more pronounced at low temperatures. A shift of the maximum peak of Z'' to a higher frequency is also observed with increasing temperature [88]. This maximum angular frequency defines the highest relaxation time τ_m from the condition $2\pi\tau f_{\max} = 1$. These results demonstrate the semiconducting nature of the heterostructure and the contribution of carriers to the relaxation process [63].

The variation of the relaxation frequency at the maximum peaks of the relaxation angular frequency $\omega_m = 2\pi f_{\max}$ as a function of temperature according to the Arrhenius law is given by [89, 90]:

$$\omega_m = \omega_0 \exp \left(-\frac{E_a}{TK_B} \right) \quad (17)$$

where, ω_0 is a constant, the activation energy is E_a , K_B is the Boltzmann constant and T is the temperature.

As can be recognized from Fig. 9d, the expression $\ln(\omega_m) = f(10^3/T)$ is a linear function providing the activation energy E_a . The activation energy represents the energy required for an ion to move from one site to another. Simply defined, it is the value of the potential barrier separating two sites.

A high dependence on the activation energy suggests a thermally activated relaxation process [63, 91]. The activation energy of the Al/p-CZTS/Mo Schottky junction was found to be 2.03 eV, which is lower than those previously reported for the same junction [38].

4 Conclusion

In summary, CZTS powder was successfully prepared by the solid state reaction technique. The CZTS powder crystallizes in the kesterite phase along the (112) plane. The optical study suggests that the bandgap energy of bulk CZTS is 1.39 eV. This paper, on the other hand, provides the first electrical study using impedance spectroscopy technique on bulk CZTS material, the results suggest that the conduction process is performed by localized state hopping, which is consistent with the correlated barrier hopping model CBH. In particular, the activation energy resulting from the maximum angular relaxation frequency and the DC conductivity imply a thermally activated carrier transport mechanism in the band gap. Subsequently, Al/p-CZTS/Mo Schottky diodes were grown by thermal evaporation at 100 °C and annealed in a sulfur atmosphere at 400 °C for 30 min. Structural characterization of the Schottky diode revealed the presence of distinct peaks of CZTS kesterite with a preferential orientation along the (112) plane. The SEM micrograph exhibited dense, rough and polycrystalline surface structures. The I-V characteristics of Al/p-CZTS/Mo diode junction were investigated. The rectifying behavior

confirms a Schottky junction with a p-type absorption layer. An ideality factor of 1.53 and a series resistance of 24.30 Ω were obtained from the experimental data. The barrier height of this heterostructure ϕ_{B0} was found to be 0.689 eV. Impedance measurements reveal that the dielectric responses found can be described by an equivalent electrical circuit, in which all series resistances R_s and parallel resistances R_p decrease as temperature increases. An activation energy of 0.203 eV was found. The results obtained thus demonstrate a significant improvement in the material properties for its use in devices, in particular a good surface morphology, a higher crystallinity and an interesting electrical conductivity. This research needs to be further developed in order to validate its relevance. Nevertheless, it has certainly revealed its relevance as a preliminary study.

Author contributions MS: investigation, methodology, writing. AH: methodology. NJ-R: review and editing. MK: supervision, validation.

Funding The authors did not receive support from any organization for the submitted work.

Data availability Not applicable.

Declarations

Conflict of interest The authors have no financial or proprietary interests in any material discussed in this article.

Ethical standards This material is the authors' own original work, which has not been previously published elsewhere. The authors declare that this article does not contain any studies involving human participants performed by any of the authors. The results are appropriately placed in the context of prior and existing research.

Research data policy and data availability statements Data sharing not applicable to this article as no datasets were generated or analysed during the current study.

References

1. N.G. Dhere, *Sol. Energy Mater. Sol. Cells* **91**, 1376 (2007)
2. N. G. Dhere, in *Sol. Energy Mater. Sol. Cells* (2011), pp. 277–280.
3. E.M. Mkawi, K. Ibrahim, M.K.M. Ali, K.M.A. Saron, M.A. Farukh, N.K. Allam, *J. Mater. Sci. Mater. Electron.* **26**, 222 (2015)
4. T. Kato, J.L. Wu, Y. Hirai, H. Sugimoto, V. Bermudez, *IEEE J. Photovoltaics* **9**, 325 (2019)
5. M.A. Green, *Prog. Photovoltaics Res. Appl.* **14**, 383 (2006)
6. B. A. Andersson, C. Azar, J. Holmberg, and S. Karlsson, *MATERIAL CONSTRAINTS FOR THIN-FILM SOLAR CELLS* (1998).
7. S. Ahmed, K.B. Reuter, O. Gunawan, L. Guo, L.T. Romankiw, H. Deligianni, *Adv. Energy Mater.* **2**, 253 (2012)
8. Q. Guo, H.W. Hillhouse, R. Agrawal, *J. Am. Chem. Soc.* **131**, 11672 (2009)
9. G. El Fidha, N. Bitri, S. Mahjoubi, M. Abaab, I. Ly, *Mater. Lett.* **215**, 62 (2018)
10. S. Biyik, F. Arslan, M. Aydin, *J. Electron. Mater.* **44**, 457 (2015)
11. S. Biyik, M. Aydin, *Acta Phys. Pol. A* **131**, 339 (2017)

12. C. Steinhagen, M.G. Panthani, V. Akhavan, B. Goodfellow, B. Koo, B.A. Korgel, *J. Am. Chem. Soc.* **131**, 12554 (2009)
13. Y.H. Khattak, F. Baig, H. Toura, S. Beg, B.M. Soucase, *J. Mater. Sci.* **54**, 14787 (2019)
14. O. Güler, T. Varol, Ü. Alver, S. Biyik, *Adv. Powder Technol.* **32**, 2873 (2021)
15. S. Biyik, *Mater. Focus.* **7**, 535 (2018)
16. S. Biyik, M. Aydin, *Acta Phys. Pol. A* **127**, 1255 (2015)
17. A.-J. Cheng, M. Manno, A. Khare, C. Leighton, S.A. Campbell, E.S. Aydil, *J. Vac. Sci. Technol. A Vacuum Surfaces Film.* **29**, 051203 (2011)
18. H. Katagiri, in *Thin Solid Films* (2005), pp. 426–432.
19. S. Zhu, J. Chen, M.F. Li, S.J. Lee, J. Singh, C.X. Zhu, A. Du, C.H. Tung, A. Chin, D.L. Kwong, *IEEE Electron Device Lett.* **25**, 565 (2004)
20. R. H. Williams, (1985).
21. A.A. Al Hattami, J.R. Rathod, E.A. Kadesh, H.S. Patel, K.D. Patel, V.M. Pathak, *Int. J. Technol.* **2**, 121 (2013)
22. S. Biyik, *Acta Phys. Pol. A* **135**, 778 (2019)
23. S. Biyik, *J. Nanoelectron. Optoelectron.* **7**, 1010 (2019)
24. S. Biyik, M. Aydin, *Acta Phys. Pol. A* **129**, 656 (2016)
25. S. Biyik, *Acta Phys. Pol. A* **132**, 886 (2017)
26. S. Biyik, *Acta Phys. Pol. A* **134**, 208 (2018)
27. S. Biyik, M. Aydin, *Acta Phys. Pol. A* **132**, 909 (2017)
28. T.K. Lin, S.J. Chang, Y.Z. Chiou, C.K. Wang, S.P. Chang, K.T. Lam, Y.S. Sun, B.R. Huang, *Solid State Electron.* **50**, 750 (2006)
29. A. R. Brown, C. P. Jarrett, D. M. De Leeuw, and M. Matters, *Field-Effect Transistors Made from Solution-Processed Organic Semiconductors* (1997).
30. I. E. Itoh and K. Miyairi, in *Thin Solid Films* (2006), pp. 95–103.
31. S. Chand, J. Kumar, *J. Appl. Phys.* **82**, 5005 (1997)
32. V. Nadenau, U. Rau, A. Jasenek, H.W. Schock, *J. Appl. Phys.* **87**, 584 (2000)
33. E. Schlenker, V. Mertens, J. Parisi, R. Reineke-Koch, M. Köntges, *Phys. Lett. Sect. A Gen. At. Solid State Phys.* **362**, 229 (2007)
34. B. Theys, T. Klinkert, F. Mollica, E. Leite, F. Donsanti, M. Jubault, D. Lincot, *Phys. Status Solidi Appl. Mater. Sci.* **213**, 2425 (2016)
35. C.L. Chan, I. Shih, *J. Appl. Phys.* **68**, 156 (1990)
36. H. Tecimer, S. Aksu, H. Uslu, Y. Atasoy, E. Bacaksiz, Ş Altindal, *Sensors Actuators A Phys.* **185**, 73 (2012)
37. Y. Atasoy, M.A. Olgar, E. Bacaksiz, *J. Mater. Sci. Mater. Electron.* **30**, 10435 (2019)
38. R. Touati, I. Trabelsi, M. Ben Rabeh, M. Kanzari, *J. Mater. Sci. Mater. Electron. Mater. Sci. Mater. Electron.* **28**, 5315 (2017)
39. P.R. Ghediya, Y.M. Palan, D.P. Bhangadiya, I.I. Nakani, T.K. Chaudhuri, K. Joshi, C.K. Sumesh, J. Ray, *Mater. Today Commun.* **28**, 102697 (2021)
40. S. Supriya, *J. Solid State Chem.* **308**, 122940 (2022)
41. S. Supriya, *Micron* **162**, 103344 (2022)
42. S. Supriya, *J. Inorg. Organomet. Polym. Mater.* **32**, 3659 (2022)
43. S. Supriya, *J. Rare Earths* **41**, 331 (2023)
44. F.Z. Boutebakh, M.L. Zeggar, N. Attaf, M.S. Aida, *Optik (Stuttg.)* **144**, 180 (2017)
45. S. Supriya, *J. Inorg. Organomet. Polym. Mater.* **33**, 3013 (2023)
46. H. Oueslati, K. Nefzi, M. Ben Rabeh, M. Kanzari, *Mater. Lett.* **273**, 127908 (2020)
47. N. Oulmi, A. Bouloufa, A. Benhaya, R. Mayouche, *Mater. Renew. Sustain. Energy.* (2019). <https://doi.org/10.1007/s40243-019-0151-2>
48. M. Sebai, I. Trabelsi, M. Kanzari, *Mater. Sci. Eng. B Solid-State Mater. Adv. Technol.* **240**, 55 (2019)
49. A. Hannachi, N. Khemiri, M. Kanzari, *J. Mater. Sci. Mater. Electron.* **33**, 20604 (2022)
50. D.B. Khadka, J. Kim, *J. Phys. Chem. C* **118**, 14227 (2014)
51. P. Bonazzi, L. Bindi, G.P. Bernardini, S. Menchetti, *Can. Mineral.* **41**, 639 (2003)
52. S. Schorr, H.-J. Hoebler, M. Tovar, *Eur. J. Mineral.* **19**, 65 (2007)
53. M. Sebai, G. Bousselmi, J.L. Lazzari, M. Kanzari, *Mater. Today Commun.* **35**, 105558 (2023)
54. P.A. Fernandes, P.M.P. Salomé, A.F. da Cunha, *Thin Solid Films* **517**, 2519 (2009)
55. X. Fontané, V. Izquierdo-Roca, E. Saucedo, S. Schorr, V.O. Yukhymchuk, M.Y. Valakh, A. Pérez-Rodríguez, J.R. Morante, *J. Alloys Compd.* **539**, 190 (2012)
56. L. Yang and B. Rn Kruse, *Revised Kubelka-Munk Theory. I. Theory and Application* (2004).
57. A. Hannachi, H. Oueslati, N. Khemiri, M. Kanzari, *Opt. Mater. (Amst.)* **72**, 702 (2017)
58. Z. Shadrokh, A. Yazdani, H. Eshghi, *Semicond. Sci. Technol. Sci. Technol.* **31**, 045004 (2016)
59. K. MijasamBattoo, *Phys. B Condens. Matter* **406**, 382 (2011)
60. S. Supriya, *Mater. Chem. Phys.* **33**, 1 (2022)
61. S. Supriya, *Mater. Res. Bull.* **96**, 290 (2017)
62. S. Supriya, Antonio J Dos Santos-García And F Fernández-Martínez, *Bull. Mater. Sci.* **39**, 85 (2016)
63. F. Borsa, D. R. Torgeson, S. W. Martin, and H. K. Patel, *Relaxation and Suctuations in Glassy Fast-Ion Conductors: Wide-Frequency-Range NMR and Conductivity Measurements* (n.d.).
64. R.M. Hill, A.K. Jonscher, DC and AC conductivity in hopping electronic systems. *J. Non-Cryst. SolidsNon-Cryst. Solids* **32**, 53–69 (1979). (North-Holland Publishing Company)
65. A.K. Jonscher, Review article, The universal dielectric response. *Nature* **267**, 673–679 (1977)
66. Jonscher, A. K. (1981). Review A new understanding of the dielectric relaxation of solids. In *JOURNAL OF MATERIALS SCIENCE* (Vol. 16).
67. R. Ondo-Ndong, G. Ferblantier, F. Pascal-Delannoy, A. Boyer, A. Foucaran, *Microelectronics J.* **34**, 1087 (2003)
68. C.P. Chan, H. Lam, C. Surya, *Sol. Energy Mater. Sol. Cells* **94**, 207 (2010)
69. M.A. Olgar, J. Klaer, R. Mainz, S. Levenco, J. Just, E. Bacaksiz, T. Unold, *Thin Solid Films* **615**, 402 (2016)
70. J.J. Scragg, T. Ericson, T. Kubart, M. Edoff, C. Platzer-Björkman, *Chem. Mater.* **23**, 4625 (2011)
71. D.B. Mitzi, O. Gunawan, T.K. Todorov, K. Wang, S. Guha, *Sol. Energy Mater. Sol. Cells* **95**, 1421 (2011)
72. S. Supriya, *J. Korean Ceram. Soc.* **60**, 451 (2023)
73. S. Supriya, *Coord. Chem. Rev.* **479**, 215010 (2023)
74. N.V. Giridharan, S. Supriya, *Thin Solid Films* **516**, 5244 (2008)
75. J.J. Scragg, J.T. Wätjen, M. Edoff, T. Ericson, T. Kubart, C. Platzer-Björkman, *J. Am. Chem. Soc.* **134**, 19330 (2012)
76. M. Ohring, *Laser-Induced Damage Opt. Mater.* **1993**(2114), 624 (1994)
77. P.A. Fernandes, P.M.P. Salomé, A.F. Sartori, J. Malaquias, A.F. Da Cunha, B.A. Schubert, J.C. González, G.M. Ribeiro, *Sol. Energy Mater. Sol. Cells* **115**, 157 (2013)
78. B.L. Guo, Y.H. Chen, X.J. Liu, W.C. Liu, A.D. Li, *AIP Adv. Adv.* (2014). <https://doi.org/10.1063/1.4861207>
79. K.V. Gurav, S.W. Shin, U.M. Patil, M.P. Suryawanshi, S.M. Pawar, M.G. Gang, S.A. Vanalakar, J.H. Yun, J.H. Kim, *J. Alloys Compd.* **631**, 178 (2015)
80. D.K. Schroder, L.G. Rubin, *Phys. Today* **44**, 107 (1991)
81. J.H. Werner, H.H. Güttler, *J. Appl. Phys.* **69**, 1522 (1991)
82. V. L. Devi, I. Jyothi, V. R. Reddy, and C.-J. Choi, *Schottky Barrier Parameters and Interfacial Reactions of Rapidly Annealed Au/Cu Bilayer Metal Scheme on N-Type InP* (2012).
83. A.E. Rakhshani, S. Thomas, *J. Electron. Mater.* **44**, 4760 (2015)
84. S.K. Cheung, N.W. Cheung, *Appl. Phys. Lett.* **49**, 85 (1986)
85. G. Güler, Ö. Güllü, Ş Karataş, Ö.F. Bakkalolu, *J. Phys. Conf. Ser. Phys. Conf. Ser.* **153**, 012054 (2009)

86. B. Roy, S. Chakrabarty, O. Mondal, M. Pal, A. Dutta, *Mater Charact* **70**, 1 (2012)
87. P.A. Fernandes, A.F. Sartori, P.M.P. Salomé, J. Malaquias, A.F. Da Cunha, M.P.F. Graça, J.C. González, *Appl. Phys. Lett. Phys. Lett.* (2012). <https://doi.org/10.1063/1.4726042>
88. S. Alialy, H. Tecimer, H. Uslu, and Ş. Altindal, *J. Nanomedicine Nanotechnol.* **04**, 1000167 (2013). <https://doi.org/10.4172/2157-7439.1000167>
89. C. Ostos, L. Mestres, M.L. Martínez-Sarrión, J.E. García, A. Albareda, R. Perez, *Solid State Sci.* **11**, 1016 (2009)
90. S. Hamrouni, M.F. Boujmil, K. Ben Saad, *Adv. Mater. Phys. Chem.* **04**, 224 (2014)
91. G. Bousselmi, N. Khemiri, A. Benali, M.P.F. Graca, R.F. Santos, B.F.O. Costa, M. Kanzari, *J. Mater. Sci. Mater. Electron.* **31**, 18858 (2020)

Publisher's Note Springer Nature remains neutral with regard to jurisdictional claims in published maps and institutional affiliations.

Springer Nature or its licensor (e.g. a society or other partner) holds exclusive rights to this article under a publishing agreement with the author(s) or other rightsholder(s); author self-archiving of the accepted manuscript version of this article is solely governed by the terms of such publishing agreement and applicable law.